Dynamic properties of structural transition in iron under uniaxial compression

2009 J. Phys.: Condens. Matter 21 245703

(http://iopscience.iop.org/0953-8984/21/24/245703)

IOP PUBLISHING JOURNAL OF PHYSICS: CONDENSED MATTER

J. Phys.: Condens. Matter **21** (2009) 245703 (7pp) doi:10.1088/0953-8984/21/24/245703

Dynamic properties of structural transition in iron under uniaxial compression

J L Shao, S Q Duan, A M He, C S Qin and P Wang

Institute of Applied Physics and Computational Mathematics, PO Box 8009, Beijing 100088, People's Republic of China

E-mail: shao_jianli@iapcm.ac.cn

Received 2 March 2009, in final form 30 April 2009
Published 26 May 2009
Online at stacks.iop.org/JPhysCM/21/245703

Abstract

By using molecular dynamics simulations, we have successfully simulated the bcc → hcp structural transition in single-crystal iron under isothermal compression along the [001] direction. The results reveal a distinct softening of C_{33} and a hardening of C_{31} (or C_{32}) prior to the transition and an over-relaxation of the stress after transition. Above the critical stress the morphology evolution of structural transition is analyzed, which can be divided into four stages: hcp homogeneously nucleated, columnar grains formed, nuclei competed and merged, and a laminar structure formed along {110} planes. Besides, our simulations demonstrate that in mixed phases the hcp phase has negative shear stress and the potential of the hcp phase is higher than the bcc phase, and the shear stress of the system keeps a linear decrease with hcp mass fraction. The effect of temperature on the structural transition is also discussed.

(Some figures in this article are in colour only in the electronic version)

1. Introduction

It is well known that the structural transition can cause an abrupt change of a material's physical and mechanical characteristics, which brings about a difficulty in understanding the dynamic response of phase-change materials. For this reason, a great deal of work has been concentrated on transition research. One of the best studied examples is the structural transition in iron. Under a high pressure of about 13 GPa, iron can undergo a representative martensitic transformation (from bcc to hcp) of no atom diffusion. Also, iron is an important structural material in applications and a main element inside the Earth's outer core [1]. Therefore, since being discovered by Bancroft *et al* [2], the structural transition in iron has been an interesting subject in high pressure research, including experimental and theoretical investigations [3–14]. For example, in 1961, Johnson *et al* studied the temperature dependence of phase transformations in iron and observed the triple point of iron [3]; in 1991, research on the hysteresis of this transition was reported [6]; in 1997, Boettger and Wallace presented an extensive study of metastability and dynamics of the structural transition [7]; and in a recent paper the influence of shear stresses on the transition was investigated theoretically based on a multiscale model [10].

However, the phase transition is not only a transdisciplinary problem related to physics, mechanics and materials science, but a multiscale problem from the discrete microstructure to the macroscopic change. In other words, the transition behavior of the material is strongly determined by the microscopic constituents of materials (atoms and the interactions among them). At present, the classical theoretical studies encounter many difficulties in understanding the nature of the phase transition. For instance, the critical pressure of the transition is still not very certain, reported in the range of 8.6–15 GPa [6], and the reverse transition starts at pressures from 16 GPa to less than 10 GPa [11]. Another puzzle is how to describe the transition interval and the mechanical response. To further understand these phenomena, the nucleation and growth of the new phase at the atomic level, as well as the interactions with external factors, have to be clarified.

Fortunately, with the rapid development in computer capability, it has been possible to simulate the above complicated phenomena. In 2002, the bcc → hcp transition in iron under shock compression was successfully observed at

the atomistic level by Kadau *et al* with molecular dynamics (MD) simulations [13]; in 2005, the results were confirmed by Kalantar *et al* via ultra-fast *in situ* x-ray diffraction studies of iron [15]; recently, Kadau *et al* simulated the shock waves in poly-crystalline iron, analyzing the effect of shock strength and grain orientation on the close-packed phase. These research works enrich our knowledge of the structural phase transformation, and also indicate that MD simulation has become a powerful tool to detect atomic-scale details in transition investigations.

In this paper, to further know the dynamic properties of the structural transition, we have performed MD simulations on the uniaxial compression process of bcc iron at constant 60 K and 300 K, respectively. First, we calculate the stresses and the elastic constants, discussing the variation of elastic constants and the over-relaxation of stresses after the phase transition. Then, we demonstrate the micro-process of hcp nucleation and growth, and give some analysis of the morphology and evolution. The radial distribution function (RDF) analysis on the transition is also presented. Finally, we present the distribution of potential energy and shear stress in mixed phase, and give the relationship of hcp mass fraction and mechanical quantities.

2. Model and simulation method

Every particle in an MD system follows Newtonian mechanics. The interaction potential between atoms plays a very important role, which determines whether the simulated results are credible. The embedded-atom-method (EAM) potential, first presented in 1983 by Daw and Baskes [16, 17], based on the density functional theory, can describe successfully the interaction between the atoms in many metals. In this work, we adopt the EAM potential introduced by Voter–Chen [18], which has succeeded in simulating the shock-induced phase transition (from bcc to hcp) of iron [13, 19, 20]. The whole potential energy of the system can be written as

$$E = \frac{1}{2}\sum_{i\neq j}\phi(r_{ij}) + \sum_{i} F_i(\rho_i), \tag{1}$$

where r_{ij} is the distance between atoms i and j, and ϕ is the corresponding pair potential. $F(\rho_i)$ represents the embedding energy of atom i, which is only dependent on the total electron density at site i.

The pair potential is taken to a Morse potential

$$\phi(r) = \alpha\{1 - \exp[-\gamma(r-\beta)]\}^2 - \alpha, \tag{2}$$

and the electron density $\rho(r)$ is taken as

$$\rho(r) = r^6[\exp(-\varepsilon r) + 2^9\exp(-2\varepsilon r)], \tag{3}$$

where $\alpha = 0.6321$ eV, $\beta = 2.029$ Å and $\gamma = 1.343$ Å^{-1} represent the depth, distance to the minimum and a measure of the curvature at the minimum, respectively; $\varepsilon = 6.262$ Å^{-1} is an adjustable parameter. The cutoff distance for this potential is 4.524 Å. Here, the embedding energy is determined numerically by the Rose equation of state [21]:

$$E_c = -E_0(1+a^*)\exp(-a^*), \tag{4}$$

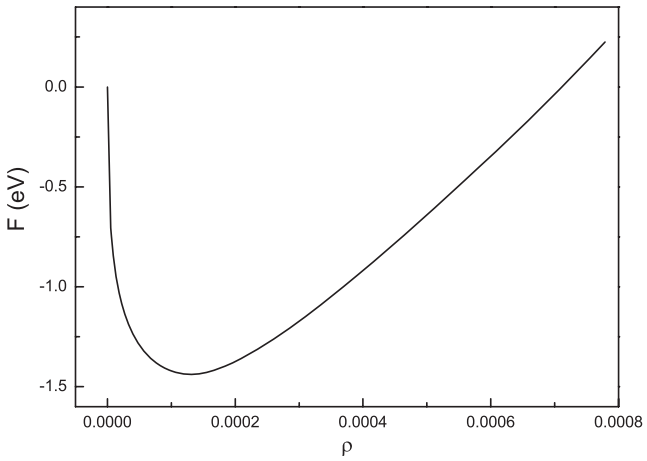

Figure 1. Variation of the embedding energy F with the electric density ρ, determined numerically by the Rose equation of state [21].

where $a^* = (a/a_0 - 1)/\sqrt{E_0/(9B\Omega)}$. a is the lattice constant, the equilibrium lattice constant $a_0 = 2.87$ Å, the cohesive energy $E_0 = 4.28$ eV, the bulk modulus $B = 173$ GPa and Ω represents the equilibrium atomic volume. Then, using the above parameters, variation of the embedding energy F with electron density ρ can be obtained, as shown in figure 1.

We selected two samples of single-crystal iron (S1 and S2). S1 consists of 350 000 atoms, with lengths $L_x = 50a$, $L_y = 50a$ and $L_z = 70a$, at a temperature of 60 K; S2 comprises 501 760 atoms, and L_x, L_y and L_z are $56a, 56a$ and $80a$ at 300 K. The x, y and z axes represent the [100], [010] and [001] directions, respectively; and periodic boundary conditions were employed in all three directions. Here, we disregard the effects of the boundary condition and the simulation scale.

A velocity Verlet algorithm [22] was selected to integrate the motion equations of the interacting particles with a time step of 2 fs. Before loading, the sample was equilibrated by means of velocity rescaling at 60 K (300 K), with a lattice constant $a = 2.8725$ Å ($a = 2.8827$ Å) chosen to set the system to be about zero pressure. Then uniaxial compression was applied by contracting the edge along the [001] direction from L_z to $0.8L_z$ at constant temperature step by step, and each contraction was held for enough time to make the sample reach equilibrium. The whole simulation time was 160 ps for S1 and 220 ps for S2.

Here, the phase transition is mainly from the bcc to hcp structure. The structural change of each atom can be judged by the centrosymmetry parameter, which is defined as follows [23]:

$$\delta = \sum_{i=1,4} |\mathbf{R}_i + \mathbf{R}_{i+4}|^2, \tag{5}$$

where $\mathbf{R}_i$ and $\mathbf{R}_{i+4}$ are the vectors corresponding to the four pairs of opposite nearest neighbors in the initial bcc lattice. The structural transition process of the whole sample is also analyzed by the radial distribution function $g(r)$. The compressive stress tensor, including longitudinal

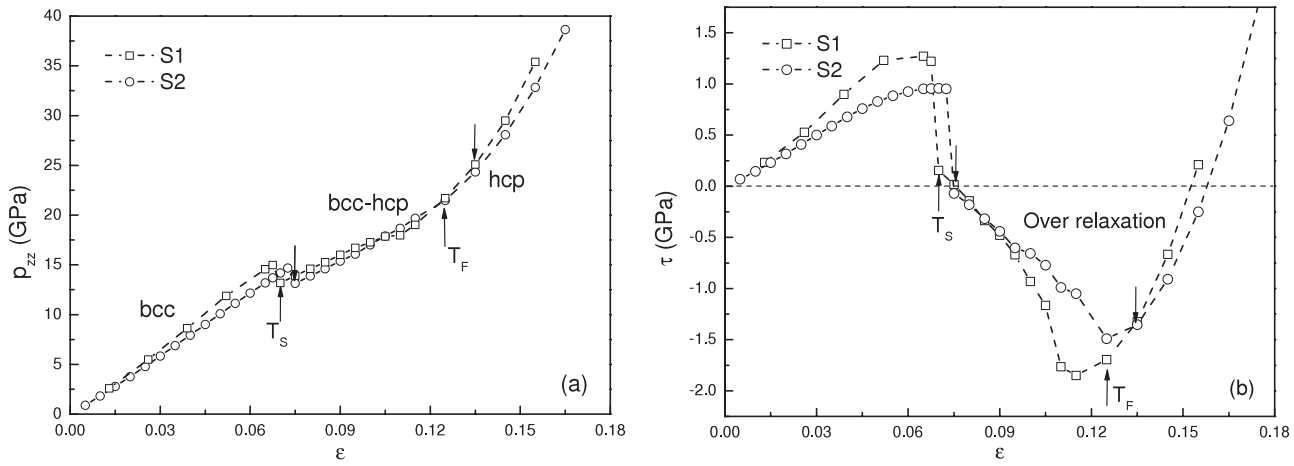

Figure 2. Variation of (a) longitudinal stress p_{zz} and (b) shear stress τ with the strain ε, where $\tau = (p_{zz} - (p_{xx} + p_{yy})/2)/2$. T_s and T_F denote the beginning and ending of the structural transition. S1: 60 K; S2: 300 K. The results are calculated according to equation (6). Curve τ of S2 is always below that of S1, until the occurrence of the phase transition, indicating that increasing temperature can soften the shear stress τ and lower the critical value for this transition.

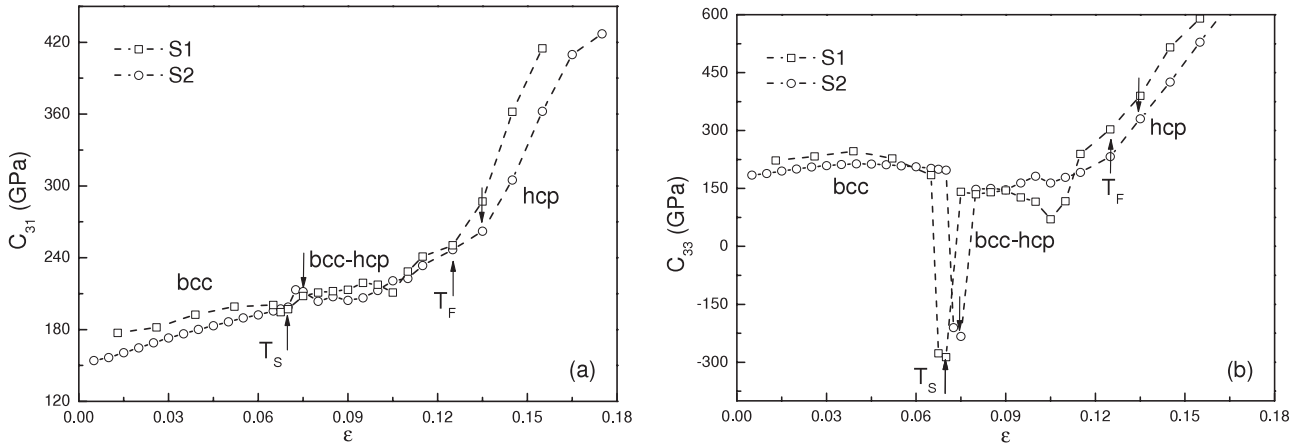

Figure 3. Variation of the elastic constants (a) C_{31} and (b) C_{33} with the strain ε. C_{31} maintaining an increase through bcc phase, reflecting the hardening of C_{31}; while C_{33}, after reaching a maximum, begin to soften. All the above elastic constants undergo a distinct hardening in hcp phase.

and transverse stresses, is calculated according to the virial formula [24, 25]:

$$p_{\alpha\beta} = \frac{1}{V}\left(\sum_i m_i v_{i\alpha} v_{i\beta} + \sum_i \sum_{i>j} r_{ij\alpha} f_{ij\beta}\right), \qquad (6)$$

where the summation is over all atoms and $\alpha(\beta)$ represent x, y or z axes. The first term in the stress tensor is the momentum flow of atoms i, whose mass and velocity are represented by m_i and v_i, respectively. The second term is the microscopic virial potential stress.

3. Results and discussion

3.1. Stress–strain analysis

To begin with, we perform the stress analysis during the compressive process. The calculated principal stress p_{zz} as a function of compression strain ε is shown in figure 2(a), where $\varepsilon = (V_0 - V)/V_0$ and V_0 denotes the initial volume of the sample. As can be seen, the stress p_{zz} discontinues near site T_s, where the value of p_{zz} jumps from ∼15 to ∼13 GPa. Namely, the critical stress p_{zz} of the transition is about 15 GPa ($\varepsilon = 0.065$), which is consistent with the result under shock loading [13]. While ε is contracted to 0.065, the bcc phase becomes unstable and more stable hcp grains appear, resulting in the abrupt change of stress p_{zz}. We also find in figure 2(a) that the value of p_{zz} for S1 is slightly higher than S2, and the latter's transition interval shifts rightward, indicating that the temperature retards the phase transition in strain. Figure 2(b) shows the change of shear stress $\tau[\equiv(p_{zz} - (p_{xx} + p_{yy})/2)/2]$. The critical shear stress τ of the structural transition for the two samples is apparently different: about 1.25 GPa for S1 and less than 1 GPa for S2. From these results, we can easily infer that increasing the temperature lowers the threshold of τ for this structural transition. Meanwhile, an over-relaxation state of the stress after T_s is found, that is to say, the value of τ becomes negative after the transition. This is because for the $(0001)_{hcp}$

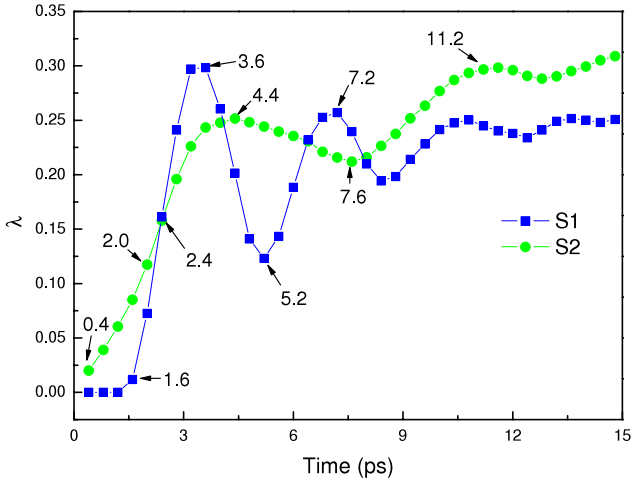

Figure 4. Time evolution of hcp mass fraction λ. The blue and green lines correspond to S1 ($\varepsilon = 0.07$) and S2 ($\varepsilon = 0.075$), respectively. Obvious oscillations of λ are shown. The oscillating period of λ in S1 is shorter than that in S2, and the maximal amplitude in S1 is bigger than that in S2. The above oscillations reflect the interaction between the nuclei.

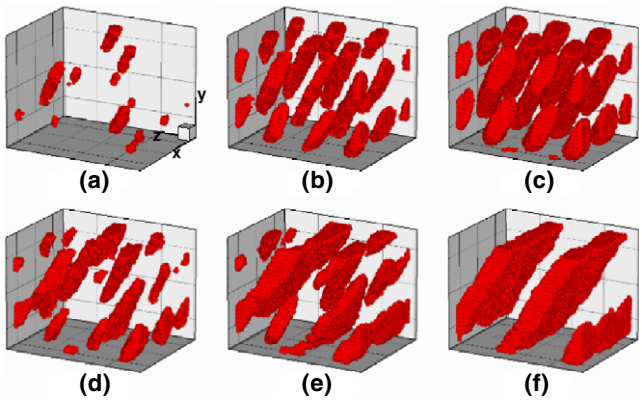

Figure 5. Morphology evolution of the hcp phase in S1 with $\varepsilon = 0.07$. The panels show snapshots at different times: (a) 1.6 ps, (b) 2.4 ps, (c) 3.6 ps, (d) 5.2 ps, (e) 7.2 ps and (f) 20 ps. Here, only the hcp atoms (with $\delta > 2$) are displayed. Homogeneous nucleation (a), columnar grains ((b), (c)), competition ((d), (e)) and laminar structure (f) are presented.

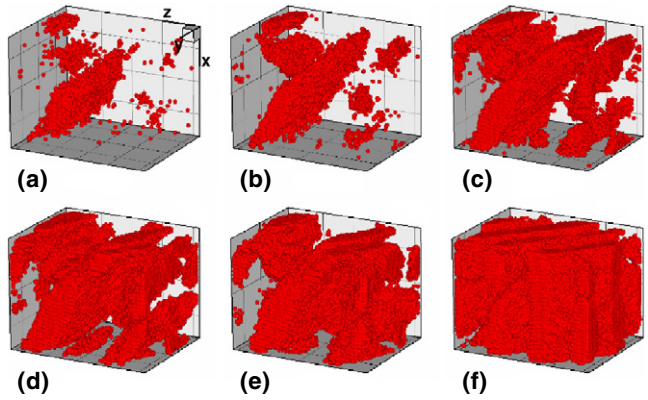

Figure 6. Morphology evolution of hcp phase in S2 for $\varepsilon = 0.075$. Different from S1, flaky morphology forms quickly after homogeneously nucleating and exhibits a cannibal growth. The times for different snapshots are: (a) 0.4 ps, (b) 2.0 ps, (c) 4.4 ps, (d) 7.6 ps, (e) 11.2 ps and (f) 28 ps.

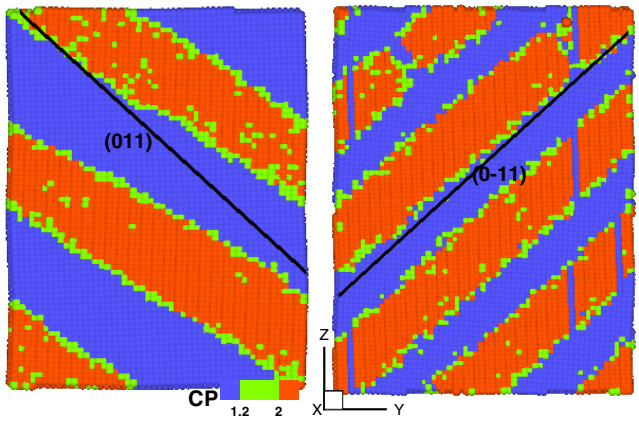

Figure 7. Snapshots of the atoms comprising one (100) plane in S1 (left, $\varepsilon = 0.08$) and S2 (right, $\varepsilon = 0.09$). The bcc phase, grain boundary and hcp phase are shown by the blue atoms, green atoms and red atoms, respectively. A laminar structure along {110} planes in mixed phases is displayed.

planes into which the $(001)_{bcc}$ planes are transforming, the crystal axis $a1$ (along the $[001]_{bcc}$ direction) is longer than the other two crystal axes $a2$ and $a3$ in the $(0001)_{hcp}$ plane. That over-relaxation state continues until about $\varepsilon = 0.15$.

The elastic constants are also calculated and discussed. The calculated results are shown in figure 3. Firstly, we find the value of C_{31} always increases prior to the phase transition (see figure 3(a)), which means the hardening of C_{31} in bcc iron. Also, temperature plays a softening role here, for the value of C_{31} at lower temperature (S1) is higher than that at higher temperature (S2) with the same strain ε. However, the result in figure 3(b) proves the softening of C_{33} ahead of the transition driven by strain, as C_{33} begins to experience a distinct reduction after reaching a maximum at about $\varepsilon = 0.04$. The phenomenon in S1 is more apparent than that in S2 due to the effect of temperature. Moreover, all the above elastic constants will undergo a strong increase after completing the transition. That inevitably leads to a nonlinear increase of the principal stress p_{zz} and the shear stress τ after the transition (see figure 2). In addition, the structural transition actually takes place in the metastable state (to overcome the interface energy for the initial hcp nucleation) in the strain-induced transition. The spontaneous growth of hcp will lead to the violent reduction of p_{zz} and, as a result, the elastic constant C_{33} presents negative values for the hcp early growth (see figure 3(b)).

3.2. Nucleation and growth of the hcp phase

By analyzing the slippage of atoms, we obtain the transformation mechanism that the adjacent (110) or $(1\bar{1}0)$ faces shuffling relatively along the $[1\bar{1}0]$ or [110] directions after the sample is contracted (along the [001] direction) to a critical value, which accords with the previous simulations

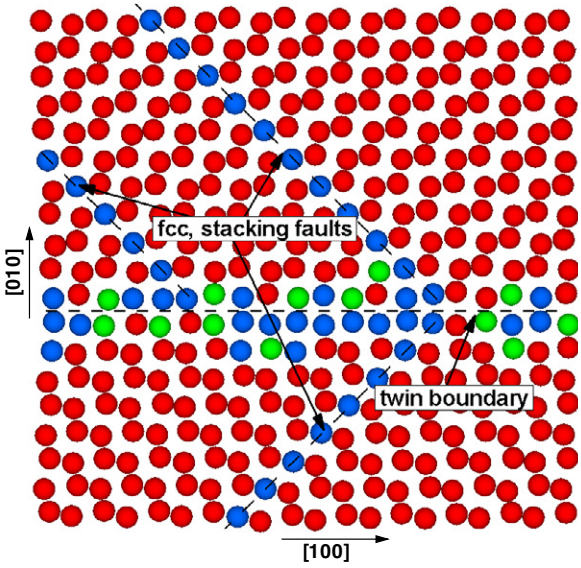

Figure 8. Atomic configuration on the (001) plane in S2 for $\varepsilon = 0.145$. Twinned boundary (along the [100] direction) and stacking faults (along the [110] and [1$\bar{1}$0] directions) are shown by the blue or green atoms.

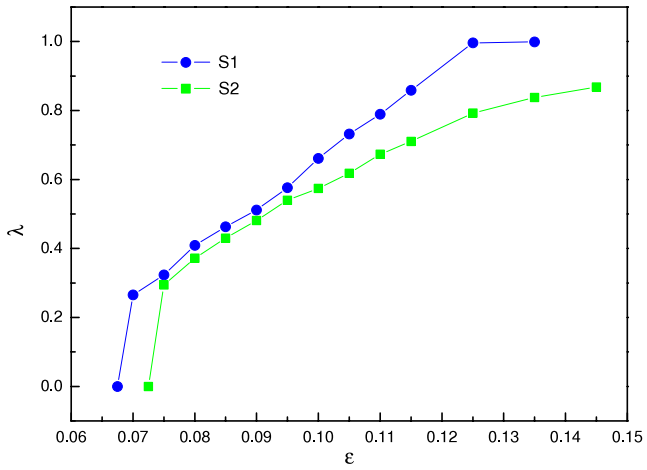

Figure 9. Variation of hcp mass fraction λ with compressive strain ε. The blue and green lines represent the results of S1 and S2, respectively. The value of λ in S1 can increase to nearly 1, while that value in S2 can only increase to less than 0.9 due to the formation of fcc structure or twinned boundaries.

under shock compression [13]. Here, we explore in detail the process of nucleation and growth. In this work, bcc and hcp phases are distinguished by the centrosymmetry parameter δ for each atom. The initial bcc structure with $\delta \leqslant 1.5$, the grain boundary with $1.5 < \delta \leqslant 2$ and the hcp structure with $\delta > 2$.

Figure 4 shows the variation of hcp mass fraction λ with time for early growth, where the blue and green lines show the calculated results for S1 ($\varepsilon = 0.07$) and S2 ($\varepsilon = 0.075$), respectively. One can see clearly the obvious oscillations of the hcp mass fraction. The blue line shows that the oscillating period of λ in sample S1 is about 3.6 ps, and the maximal amplitude is near 0.2; while the oscillating period in S2, shown by the green line, is longer than that in S1, arriving at 6.8 ps, and the maximal amplitude attenuates to 0.04. These results suggest there exist strong interactions between nuclei for the early stage. With the increase in ambient temperature, the interaction can become weak, and probably conducive to the change of the hcp growth pattern. In addition, the above oscillations weaken rapidly only in two or three periods.

The microscopic view of the initial nucleation and growth of the hcp phase for S1 and S2 are shown in figures 5 and 6, respectively. Figure 5 shows clearly four stages of hcp phase in S1 for $\varepsilon = 0.07$. At the load time of 1.6 ps, some distinct hcp grains emerge (a); these hcp grains grow quickly into columnar grains ((b), (c)), which correspond to the formation of the first peak of λ in figure 4; then, some nuclei tend to be flaky and others reduce gradually and even disappear because of the competition between hcp nuclei ((d), (e)), corresponding to the first trough of λ in figure 4. Ultimately, a laminar structure consisting of bcc and hcp iron comes into being nearly along the (011) planes.

It can be seen from figure 6 that the morphology evolution of the hcp phase in S2 ($\varepsilon = 0.075$) is very different from S1. The flaky grain forms quickly after homogeneously nucleating ((a), (b)), though with some small hcp grains in the nearby regions. At this stage, the growing manner of the hcp grain is mainly the flaky cannibal growing. As the flaky grain tends to be stable, the other small grains grow into flaky grains correspondingly (c)–(f). These results indicate that some grains exhibit first a dominant growth, while the others can only proceed by secondary growth. However, there also forms a laminar structure along the (0$\bar{1}$1) plane in the end.

Figure 7 shows that the above flaky hcp grains would broaden along the [01$\bar{1}$] or [0$\bar{1}$1] directions with increasing compression, and the habit plane is maintained nearly along the {011} planes. Ultimately, the grain boundaries either disappear or form twin boundaries: while the slipping directions of bilateral atoms are parallel, the grain boundaries would disappear; and while the slipping directions of bilateral atoms are perpendicular, the grain boundaries would form the twinned boundaries. In this work, there only appear a few stacking faults in S1, while both twins and stacking faults form in S2. In figure 8, we plot the atoms on the (001) plane in S2 after the phase transition. The twinned boundary is found along the [100] direction and stacking faults along the [110] or [1$\bar{1}$0] directions. In addition, we display the mass fraction λ of hcp in the two samples (see figure 9). It is found that the value of λ in S1 is evidently above the value in S2 after $\varepsilon = 0.1$, and λ in S2 cannot reach 1. This is because of the formation of a few twins in S2, which seems to block the late growing of the hcp grains to some extent.

3.3. Structural analysis of the samples

Structural analysis of the phase transition is analyzed by the radial distribution function (RDF). Figure 10 displays the RDFs under different compressions, where the compressive strain changes from 0 to 0.125 for S1 and from 0 to 0.135 for S2. Obviously, the RDF of a perfect bcc structure (with no lattice vibration) has five peaks in the range $r \leqslant 0.55$ nm,

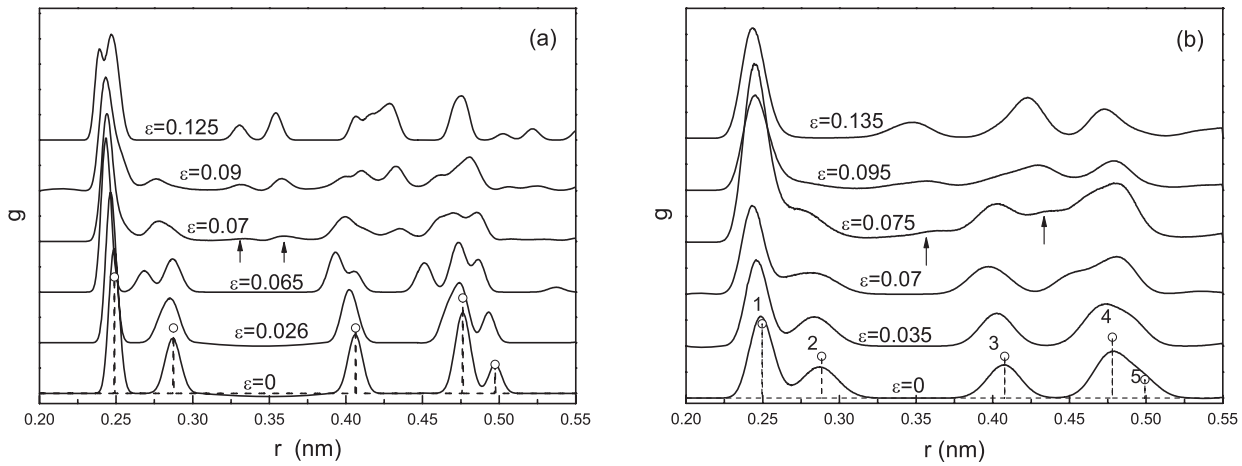

Figure 10. Radial distribution functions (RDFs) for different strains ε in (a) S1 and (b) S2. For the case of $\varepsilon = 0$ (initial structure), there are five peaks in the range $r \leqslant 0.55$ nm in S1, similar to a perfect bcc structure (marked by the circles); in S2, the fifth peak disappears and the other peaks broaden due to the temperature effect. The occurrence of the phase transition is reflected clearly by the change of the second peak of the PDFs.

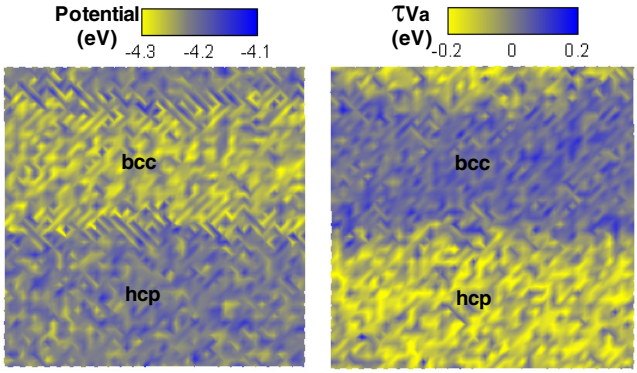

Figure 11. Distribution of potential and shear stress volume on the (001) plane in S1 for $\varepsilon = 0.08$; V_a indicates the atomic volume. Clearly, the potential of the hcp phase is higher than that of the bcc phase; the value of τV_a becomes negative in the hcp phase.

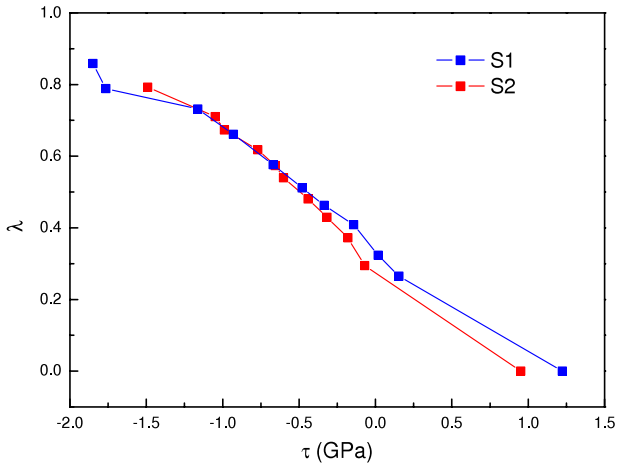

Figure 12. Variation of hcp mass fraction λ with shear stress τ. The results of S1 and S2 are shown by the blue and green lines, respectively. For both the samples, a linear decrement of τ with increasing λ is presented.

which are marked by the circles. Figure 10(a) shows that the initial configuration of S1 still has all the five peaks. Under weak compression, all the peaks shift to the left slightly; while $\varepsilon = 0.065$, the second peak shows a distinct split, because the lattice constant along [001] is contracted to a certain extent. However, while ε is above 0.07, the RDF undergoes a prominent change: the two split peaks merge into one peak and a few new peaks appear as shown by the arrows. These changes are because a certain number of atoms have transformed to the hcp structure. Figure 10(b) shows the changes of the RDF in S2. For the effect of the temperature (300 K), the peaks of RDF broaden and the fifth peak disappears due to the random vibration of atoms. Under continued compression, a shift of the peaks is observed, while the splitting of the second peak does not occur. The structural transition with the compressive strain can only make the second peak of RDF reduce gradually and even disappear.

3.4. Mechanical properties in mixed phases

In the end, we investigate the variation of the mechanical quantities with the hcp mass fraction λ through the transition interval. One can see from figure 11 that both the potential and the shear stress volume τV_a are heterogeneous in mixed phases. The potential of the hcp phase is clearly higher than that of the bcc phase; the value of τV_a in the bcc phase is positive, while the hcp phase has negative τV_a, which can make the system show an over-relaxation. Figure 12 shows the relationship between λ and τ. The shear stress τ presents a linear decrement with increasing hcp mass fraction during the whole bcc to hcp transition. It should be noted that the result of hcp mass fraction λ is affected by the judging method and the position fluctuation of atoms. Nevertheless, this cannot change the above mechanical properties and regularities.

4. Conclusion

By using the molecular dynamics method, we have successfully simulated the process of the bcc → hcp phase transition in iron under constant temperature compression (along the [001] direction). It is found that there is a distinct softening of the elastic constant C_{33} prior to the structural transition and an over-relaxation of the stress after the transition. In sample S1 (60 K), morphology evolution of the hcp phase can be divided into four stages: homogeneous nucleation, columnar growth, competition and laminar structure. In S2 (300 K), different from S1, a flaky morphology forms quickly and exhibits a cannibal growth. These grain boundaries extend along the $[01\bar{1}]$ or $[0\bar{1}1]$ directions, and ultimately disappear or form twin boundaries under increasing compression. The distribution of potential and shear stress in mixed phases for S1 is discussed, which indicates that the potential of the hcp phase is clearly higher than that of the bcc phase and the value of τV_a for the hcp phase is negative. Besides, the shear stress keeps a linear decrease with the hcp mass fraction.

Acknowledgments

This work was supported by the Foundations for Development of Science and Technology of China Academy of Engineering Physics under grant nos. 2007A09001 and 2008B0101008.

References

[1] Birch F 1952 *J. Geophys. Res.* **57** 227
[2] Bancroft D, Peterson E L and Minshall S 1956 *J. Appl. Phys.* **27** 291
[3] Johnson P C, Stein B A and Davis R S 1962 *J. Appl. Phys.* **33** 557
[4] Takahashi T and Basset W A 1964 *Science* **145** 483
[5] Barker L M and Hollenbach R E 1974 *J. Appl. Phys.* **45** 4872
[6] Taylor R D, Pasternak M P and Jeanloz R 1991 *J. Appl. Phys.* **69** 6126
[7] Boettger J C and Wallace D C 1997 *Phys. Rev.* B **55** 2840
[8] Yano K and Horie Y 2002 *Int. J. Plast.* **18** 1427
[9] Jensen B J, Rigg P A, Knudson M D, Hixson R S, Gray G T III, Sencer B H and Cherne F J 2006 *AIP Conf. Proc.* **845** 232
[10] Caspersen K J, Lew A, Ortiz M and Carter E A 2004 *Phys. Rev. Lett.* **93** 115501
[11] Caspersen K J, Lew A, Carter E A and Ortiz M 2006 *J. Mech. Phys. Solids* **54** 1276
[12] Ma Y Z, Selvi E, Levitas V I and Hashemi J 2006 *J. Phys.: Condens. Matter* **18** S1075
[13] Kadau K, Germann T C, Lomdahl P S and Holian B L 2002 *Science* **296** 1681
[14] Kadau K, Germann T C, Lomdahl P S and Holian B L 2005 *Phys. Rev.* B **72** 064120
[15] Kalantar D H *et al* 2005 *Phys. Rev. Lett.* **95** 075502
[16] Daw M S and Baskes M I 1983 *Phys. Rev. Lett.* **50** 1285
[17] Daw M S and Baskes M I 1984 *Phys. Rev.* B **29** 6443
[18] Harrison R, Voter A F and Chen S-P 1989 *Atomistic Simulation of Materials-Beyond Pair Potentials* ed V Vitek and D J Srolovitz (New York: Plenum) p 219
[19] Kadau K *et al* 2007 *Phys. Rev. Lett.* **98** 135701
[20] Shao J L, Wang P, Qin C S and Zhou H Q 2007 *Acta Phys. Sin.* **56** 5389
[21] Rose J H, Smith J R, Guinea F and Ferrante J 1984 *Phys. Rev.* B **29** 2963
[22] Swope W C, Andersen H C, Berens P H and Wilson K R 1982 *J. Chem. Phys.* **76** 637
[23] Kelchner C L, Plimpton S J and Hamilton J C 1998 *Phys. Rev.* B **58** 11085
[24] Irving J H and Kirkwood J G 1950 *J. Chem. Phys.* **18** 817
[25] Allen M P and Tildesley D J 1987 *Computer Simulations of Liquids* (Oxford: Oxford University Press) p 46